The electrode tortuosity factor: why the conventional tortuosity factor is not well suited for quantifying transport in porous Li-ion battery electrodes and what to use instead

Tuan-Tu Nguyen, Arnaud Demortière, Benoit Fleutot, Bruno Delobel, Charles Delacourt, Samuel J Cooper

npj Computational Materials

www.nature.com/npjcompumats

ARTICLE OPEN

The electrode tortuosity factor: why the conventional tortuosity factor is not well suited for quantifying transport in porous Li-ion battery electrodes and what to use instead

Tuan-Tu Nguyen[1,2], Arnaud Demortière[1,3,4], Benoit Fleutot[1,3], Bruno Delobel[2], Charles Delacourt[1,3]✉ and Samuel J. Cooper[5]✉

The tortuosity factor of porous battery electrodes is an important parameter used to correlate electrode microstructure with performance through numerical modeling. Therefore, having an appropriate method for the accurate determination of tortuosity factors is critical. This paper presents a numerical approach, based on simulations performed on numerically-generated microstructural images, which enables a comparison between two common experimental methods. Several key issues with the conventional "flow through" type tortuosity factor are highlighted, when used to characterise electrodes. As a result, a new concept called the "electrode tortuosity factor" is introduced, which captures the transport processes relevant to porous electrodes better than the "flow through" type tortuosity factor. The simulation results from this work demonstrate the importance of non-percolating ("dead-end") pores in the performance of real electrodes. This is an important result for optimizing electrode design that should be considered by electrochemical modelers. This simulation tool is provided as an open-source MATLAB application and is freely available online as part of the *TauFactor* platform.

npj Computational Materials (2020)6:123 ; https://doi.org/10.1038/s41524-020-00386-4

INTRODUCTION

Microstructure plays a crucial role in the performance of lithium-ion battery (LIB) electrodes, affecting electronic and ionic effective transport properties, electrochemical kinetics via the interfacial area between phases, as well as the mechanical properties due to the nonuniform distribution of phases. High-rate charging is of particular importance to automotive LIBs[1–4] and so the morphology of next-generation electrodes must be designed to overcome transport limitations. Physics-based models can be used to accelerate this optimization process by giving insight into the relationship between microstructure and performance. However, to ensure that the quantitative results of simulations are meaningful, accurate geometric and physical properties are needed as inputs, as well as robust validation data.

Porous electrode structures can massively increase the specific interfacial area between phases, which can be used to increase the accessible capacity of the active materials at high rates. Rather than simulating electrochemical processes directly in 3D microstructure, most battery models apply a macroscopic treatment in which only certain homogenized metrics are used to represent the geometry, and the exact geometric details are disregarded. In the widely used Newman pseudo 2-dimensional (P2D) model, for instance, the porous electrode is treated as a mixture of two phases, namely a solid phase including active material, carbon, and binder, and a liquid phase, which is the electrolyte. In the porous electrode theory, the two phases are considered as the superposition of two continua at any point in space, which are ascribed macro-homogenous parameters such as porosity ε, specific active surface area (ASA) a, and a tortuosity factor τ.[5,6] As reported in previous works, however, those parameters may in reality be inhomogeneous, and the tortuosity factor may also be anisotropic[3].

Porosity can be measured either directly, using 3D imaging techniques[7–9], indirectly, using techniques such as helium pycnometry, or inferred from knowledge of the electrode precursors along with the mass and dimensions of the finished electrode. Surface area can, in principle, be explored using imaging techniques, although resolution constraints can present a challenge and adsorption techniques like the Brunauer–Emmett–Teller (BET) method are typically preferred. Nevertheless, there can be a difference between the surface area measured with the BET method and the active surface area used in Newman's P2D model, since BET areas are a measure of the entire area available for gas adsorption and not only the electrochemically active surface area[10]. The determination of tortuosity factors presents an even greater challenge as they are an emergent global property of the microstructures' interaction with a particular transport process and, as such, require either a transport experiment or a simulation. The focus of this paper is on the determination of tortuosity factors relevant to LIB electrodes.

In this work, we use the standard definition for the tortuosity factor, τ, as stated in the following equation[11,12]:

$$\frac{\tau}{\varepsilon} = \frac{\rho_{\mathrm{eff}}}{\rho_0} = \frac{\kappa_0}{\kappa_{\mathrm{eff}}} = \frac{D_0}{D_{\mathrm{eff}}} = N_{\mathrm{M}}, \quad (1)$$

where N_{M} is the MacMullin number; ρ_0, κ_0, and D_0 are, respectively, the "intrinsic" electrical resistivity (Ω m), conductivity (S m^{-1}) and diffusion coefficient (m^2 s^{-1}) of the electrolyte; and ρ_{eff}, κ_{eff}, and D_{eff} are the observed "effective" values resulting from the transport constraints imposed by a porous (and possibly tortuous) microstructure. Equation 1 illustrates that the tortuosity

[1]Laboratoire de Réactivité et Chimie des Solides (LRCS), CNRS UMR 7314, Université de Picardie Jules Verne, Hub de l'Energie, Rue Baudelocque, 80039 Amiens Cedex, France. [2]Renault Technocentre, 78084 Guyancourt, France. [3]Réseau sur le Stockage Electrochimique de l'Energie (RS2E), CNRS FR 3459, Hub de l'Energie, Rue Baudelocque, 80039 Amiens Cedex, France. [4]ALISTORE-European Research Institute, CNRS FR 3104, Hub de l'Energie, Rue Baudelocque, 80039 Amiens Cedex, France. [5]Dyson School of Design Engineering, Imperial College London, London SW7 2DB, UK. ✉email: charles.delacourt@u-picardie.fr; samuel.cooper@imperial.ac.uk

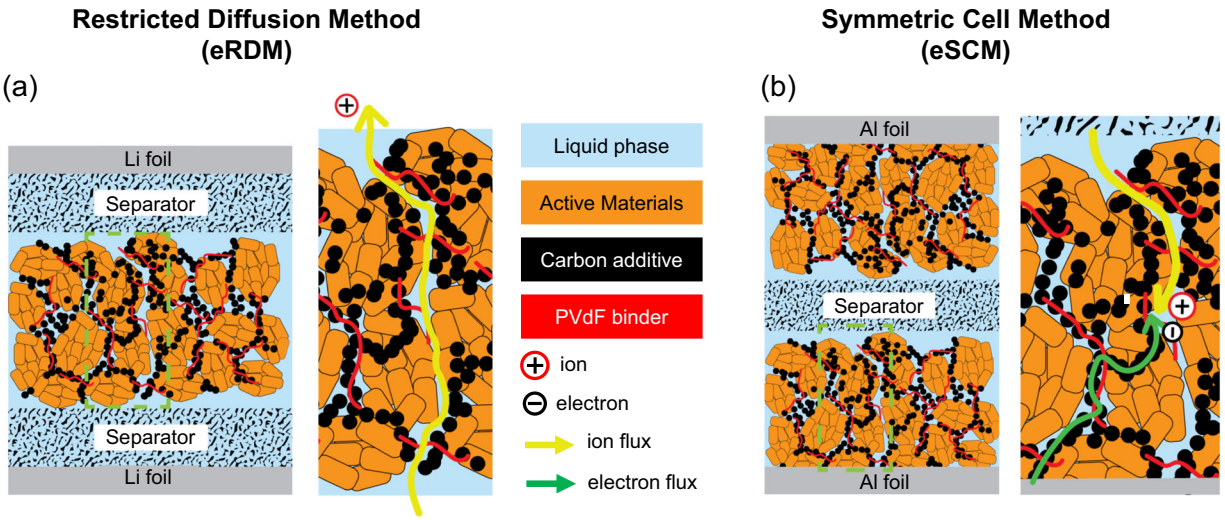

Fig. 1 Schematics of experimental setup and the physics underlying the two methods for determining tortuosity factors of porous electrodes: **a** eRDM[16], and **b** eSCM[17,18]. The arrows show different conducting pathways traveled by charged particles(ions/electrons).

factor of a porous structure can be determined based on the ratio of the effective and intrinsic transport properties. Various "geometrical tortuosities" can also be found in the literature, but these are not well suited to characterizing 3D pore networks and they suffer from key conceptual limitations such as ignoring constriction in flow paths.

The following two experimental techniques are used in the field of electrochemistry to determine the tortuosity factor of electronically insulating porous materials, such as battery separators. Both techniques require the porous medium to be infiltrated with an ionically conductive salt (of known bulk conductivity (κ_0) and diffusivity (D_0)), and then placed between two electronically conductive plates to form a cell.

The first technique is known as the "restricted-diffusion method" (RDM)[13–15] and is based on measuring diffusion in the time domain. For this technique, the plates on either side of the cell must be electroactive with respect to one of the ions in the electrolyte. A bias is applied between the plates, establishing a constant current, which in turn generates a linear salt concentration gradient across the cell. When the bias is removed, the salt gradually diffuses back to a uniform distribution, which is known as the relaxation step. By monitoring the salt diffusion during the relaxation step at sufficiently long times[14], which can be done by following the decay of the electrochemical potential at each plate, using reference electrodes, one can determine the effective salt diffusion coefficient, D_{eff}, within the porous medium. The experimental measurement of a cell potential can also be compared to a simulation with a numerical transport model to determine the effective salt diffusion coefficient within the porous medium. In the case of an infinite dilute solution, the relation between the flux and the gradient concentration can be described by Fick's law.

The second technique utilizes the frequency–domain, where the high frequency impedance response of this symmetric cell is measured (referred to as SCM for convenience in this paper). By making the assumption that this impedance is caused entirely by the migration flux passing through the electrolyte filled pores, the effective ionic conductivity of the electrolyte filled pore network, κ_{eff}, can then be calculated using Ohm's law.

Crucially, the two commonly used methods described above cannot be applied directly to electronically-conducting porous materials, such as battery electrodes. This is partly because the material would create an electronic short-circuit path between the two plates in the RDM, and because the presence of the electronic conductor would interact with the potential field with the SCM, which undermines the simplified assumptions in the analysis. However, the following two adapted versions of these methods have been proposed:

The first method was developed by Thorat et al.[16] and is a time–domain approach based on RDM, but with two key differences. The cell used for this experiment requires a "free-standing" electrode, which is typically obtained by simply peeling the porous electrode material off the current collector foil. This electrode is then placed between two separators (i.e., electronically insulating and permeable materials) to electronically isolate it, before sandwiching these three layers between two lithium foils, as shown in Fig. 1a. Similar to RDM, a bias is applied causing a steady-state current in order to establish a salt concentration distribution across the cell. The use of the transport model is preferred, as it facilitates the decorrelation of the contribution of the porous electrode layer to the overall transport from other porous layers (two separator layers). The experimental measurement of a cell potential is compared to a simulation with a numerical transport model to determine the effective salt diffusion coefficient within porous electrodes. Here, we refer to this variant of the RDM for electronic conductors as eRDM.

The second approach was developed by Landesfeind et al.[17] and Malifarge et al.[18] and, similar to SCM, it is a frequency-domain technique. It employs a conventional symmetric cell setup, as shown in Fig. 1b, where a pair of identical electrodes (backed by current collector foil) are placed either side of a separator. In order to extract information about the pore phase only, a blocking condition is imposed at the electrode surface, preventing insertion of the mobile ions. This can be achieved through either the use of a nonintercalating electrolyte salt and/or by using electrodes in a nonintercalating state (e.g., fully lithiated/delithiated). Electrochemical impedance spectroscopy (EIS) is then used to extract an impedance spectrum[19], from which information about the processes inside this cell can be extracted. A more involved analysis is required than for the simple SCM method and is described in more detail later in this article. We refer to this symmetric cell method for characterizing transport in porous electronic conductors as eSCM.

A recent comparison of these two methods for commercial battery electrodes was made by Pouraghajan et al.[20], which showed a reasonable agreement between these two approaches in cases where both of them can be implemented. Nevertheless, in many cases[20], the eSCM seems to be faster and more convenient to implement than the eRDM, which requires a current-collector-free

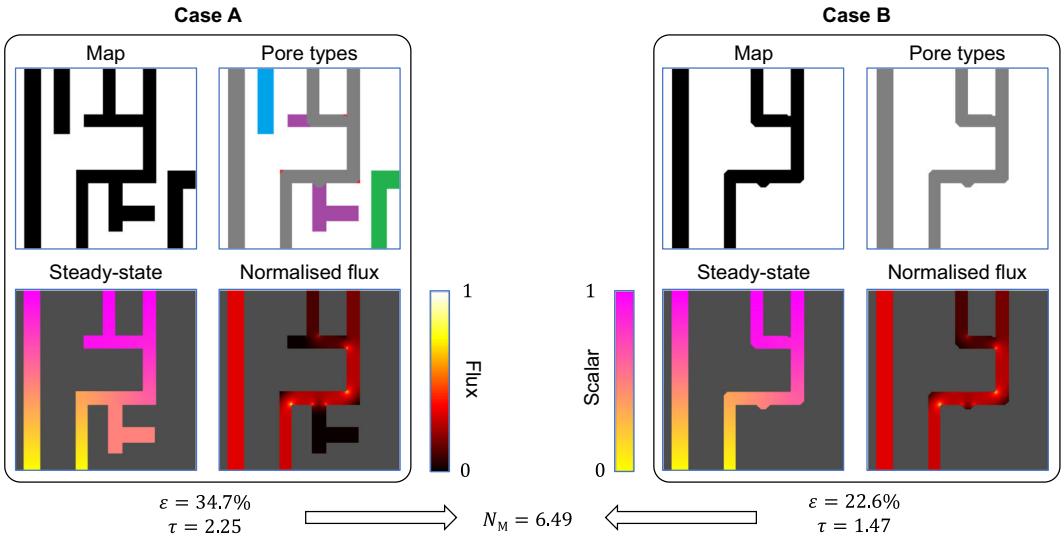

Fig. 2 Illustration of different types of pores that can be present within porous electrodes and their effects on the tortuosity factor τ and McMullin number N_M determination. The simulated steady-state scalar distributions are shown as well as the normalized flux maps. **Case A:** microstructure with five different pores types: gray—through pores; blue—dead-end pores for eRDM, that may or may not be available for eSCM, depending on the orientation of the CV; purple—dead-end pores for eRDM that branch from the through pores; green—dead-end pores like Blue but could become through pores if the CV was larger as it extends out the side of the CV; and red—small corner regions having low flux. **Case B:** microstructure with only through-pores (gray) based on low flux threshold. The microstructure size is 256 × 56 pixels.

electrode along with precise determination of the bulk diffusion coefficient of the liquid electrolyte.

Besides electrochemical methods for quantifying the tortuosity factor mentioned above, 3D imaging techniques can be used to capture the geometry of these porous electrodes at the nanoscale. Although the imaged volume is generally very small in comparison to the cell, if it is large in comparison to the pore features, then this data may still be used to extract average morphological metrics that are representative of the whole electrode. Perhaps the most commonly used tomography methods for battery materials are X-ray computed tomography (XCT)[9,21–25] and focused ion beam scanning electron microscopy (FIB-SEM)[26,27]. FIB-SEM, which is a destructive technique, often offers a higher resolution compared to XCT, but typically only a small volume can be acquired in a reasonable time. In contrast, XCT allows nondestructive imaging of the microstructure with a capability of analysing much larger volumes (although sample preparation often destroys the sample from an electrochemical perspective). However, the lack of capability in capturing either the fine features (due to the resolution) or different phases (the carbon-binder domain is rarely well captured with X-ray tomography based on attenuation contrast) in the tomographic data can be a source of errors that impacts the quantification of microstructural properties, in particular interfacial area[28,29].

Among various tools for analysing tomographic data, *TauFactor*, developed by Cooper et al.[30], is an open-source MATLAB application that calculates tortuosity factors directly from segmented image stacks, as well as volume fractions, surface areas, and other microstructural properties. To calculate the tortuosity factor, *TauFactor* uses an over-relaxed iterative approach to solve the steady-state diffusion equation of species in an infinitely dilute solution between two fixed value boundaries in a porous medium, i.e., similar to eRDM method. However, it is worth stating that this simple definition of the tortuosity factor does not account for the multiphysics processes occurring in a real electrochemical system. For example, there are no contributions to ionic transport from electric migration or convection and no double-layer formation at the solid/liquid interface[31]. It is the simplicity of this approach which allows for the system to be solved quickly, and this, in turn, has made this method of tortuosity factor determination the standard when using tomographic data.

In this paper, we develop a new frequency-domain solver within the *TauFactor* framework in order to replicate the eSCM approach and understand why it can give different results to those derived through eRDM. Specific cases of 2D and 3D microstructures are studied to showcase the crucial difference between the two methods and highlight cases, where one approach might be preferred.

RESULTS

Tortuosity factors calculated by the two approaches are denoted: τ for a tortuosity factor derived from the conventional eRDM approach and τ_e for "electrode tortuosity factor" determined using the eSCM. Furthermore, MacMullin numbers N_M and $N_{M,e}$ are defined similarly.

The conventional definition of tortuosity factor, τ, considers the steady-state flux of species from one side of the control volume (CV), through the pore network and out the opposite side. In this work, we describe pathways connecting between these two sides as "through-pores". Pores that start from the separator side and reach the current collector side would count as through-pores (i.e., the current collector is not counted as part of the porous electrode). Those pores that either do not connect across the full thickness or have negligible contribution to the steady-state diffusive flux (see Fig. 2) are denoted as "dead-end pores" and their presence would cause an increase in the value of τ.

However, in the case of battery porous electrodes, "dead-end" pores may make a significant contribution to the transport. This is because battery electrodes do not require transport all the way through the pore structure, but rather the combination of ion transport from the separator (through the liquid) to the solid/liquid interface and electron transport from the current collector (through the solid) to the solid/liquid interface. This suggests that the conventional tortuosity factor, τ, may be a misleading metric when trying to predict battery performance.

By simulating the eRDM and eSCM concepts to extract both τ and τ_e from a variety of microstructures, we will demonstrate that

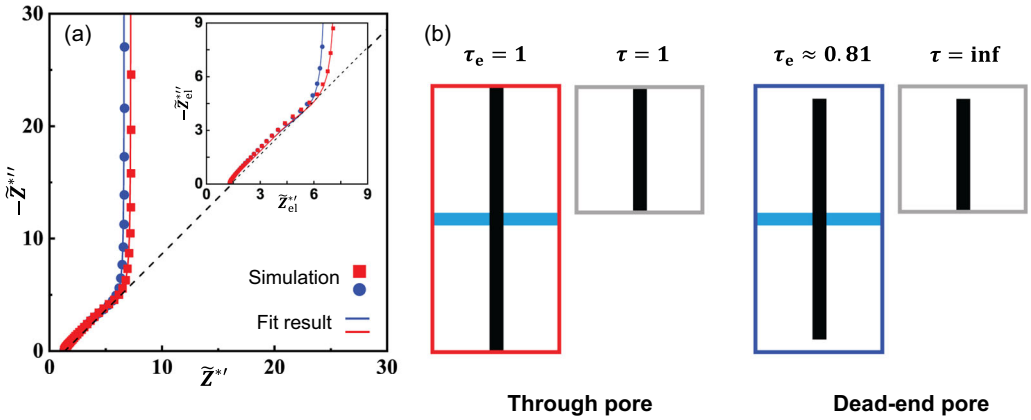

Fig. 3 Comparison of the two approaches applied to the simplest cases. a Simulated EIS of eSCM of the two 2D microstructures containing either only straight through-pores (red) or only straight dead-end pores (blue) along with the corresponding fits with Eq. 4. The inset image displays the zoom at the mid-frequency region. The 45° slope in dashed line is used to guide the eyes; **b** The geometry of two microstructures with τ_e and τ derived from the eSCM and eRDM simulations. The box color corresponds to the colors in the Nyquist plot. The light blue band in the middle of the SCM geometries represents a separator with a direct pore connecting the two sides. The microstructure size is 100 × 100 pixels, the pixel size equals 1 μm.

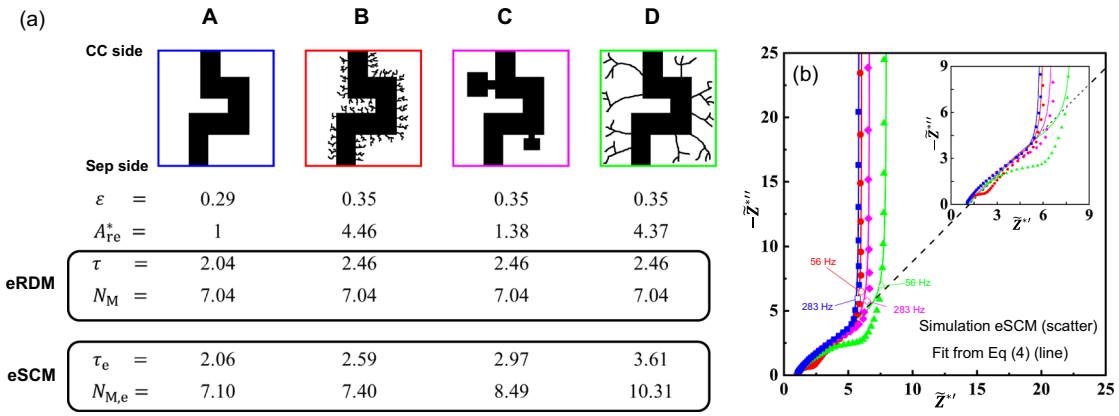

Fig. 4 Comparison of two approaches with 2D microstructures. a The four 2D microstructures are presented along with τ, N_M given by eRDM and τ_e, $N_{M,e}$ given by eSCM in each case; the current collector "CC side" and the separator "Sep side" are labeled; **b** simulated EIS of eSCM of the four microstructures along with the fit using Eq. 4, the inset graph shows a zoom on the mid-frequency region to highlight the deviation of the simulated EIS shape from the conventional TLM response. The 45° slope in dashed line is used to guide the eyes. The numerically-generated microstructure size is 300 × 300 pixels, the pixel size equals 1 μm.

τ_e is more relevant to predicting the performance of battery electrodes.

Simulations of 2D microstructures

In Fig. 2, we first consider an example to clearly showcase different types of pores that are investigated throughout this work. Based on the diffusive flux through the porous structure at steady-state (simulated with *TauFactor*), two main types of pores, as mentioned above, through pores and dead-end pores can be identified along with the quantification of their volume fraction respectively. Case A consists of both through and dead-end pores. At steady-state, only percolated pores are shown, in which there are pore regions that have a uniform concentration. Thus, these regions of pores contribute negligibly to the diffusive flux, as can be seen in the flux density map with almost no flux there. Since the diffusive flux is expected to penetrate through the porous microstructure principally by through-pores rather than dead-end pores, we apply an arbitrary threshold value (2% of maximum) to the flux density map at steady-state to label pores as "through" or "dead-end". Then, among the dead-end pores, we divided them into subclasses of pores (differentiated by color). Once every pore is labeled, case B shows a microstructure that contains only the through pores (in gray) previously presented in case A. It's interesting to note that the value of N_M is the same for cases A and B, since the transport through these two systems would be essentially the same, as the pores that were removed make a minimal contribution to transport through the system.

The difference in terms of concept and physics between the two methods, eRDM and eSCM, is first illustrated through a very simple 2D example, as shown in Fig. 3b, in which the microstructure has either only straight through-pores or only straight dead-end pores.

With only through-pores, the two approaches give the same value of 1 for the tortuosity factor, as expected for straight pores. Furthermore, this result helps to cross-check the symmetric cell model implemented in *TauFactor*. On the other hand, for a 2D structure based on a dead-end pore, the tortuosity factor values found by the two methods strongly contrast with each other: an infinite tortuosity factor results from the eRDM, whereas the eSCM yields an electrode tortuosity factor value less than 1.

Microstructures made of simple pore networks containing both through and dead-end pores are studied next, as shown in Fig. 4. The MacMullin number N_M in Eq. 1 is also reported here since it

describes the effect of a porous microstructure on the behavior of the liquid phase within the pore network[11,17,32] and as such it also appears in Newman's P2D model through the mass balance in the liquid phase and the Mac-Innes equation for ionic transport[6].

A template geometry is created in which there is only one through pore (case A in Fig. 4). Then, three other geometries (cases B, C, D) are derivatives of geometry A through adding a constant volume fraction of dead-end pores ($\varepsilon_{dead} = 6\%$). The dead-end pores are all branched from the through pore. They are intentionally made to be different in terms of morphology from one structure to another, which leads to different values of the microscopic active area, A^* (see Eq.3). The following four structures are investigated:

1. Only one main through pore and no dead-end pore (A).
2. Many short dead-end branches in addition to the main through pore (B).
3. Dead-end branches with low microstructural active surface area in addition to the main through pore (C).
4. A few long dead-end branches in addition to the main through pore (D).

The four microstructures are intentionally designed to have the same value of the conventional MacMullin number, N_M. In addition, the three derivative microstructures each have the same conventional tortuosity factor, τ, as each other. The microscopic active surface area A^* is represented as a relative value A^*_{re} to that of microstructure A for ease of comparison. The electrode tortuosity factor, τ_e, is then expected to be impacted only by the dead-end pores in different ways in each situation according to their morphology. It can lead to more pronounced discrepancies between the two methods, allowing us to unveil the fundamental difference between them.

As shown in Fig. 4a, the three geometries B, C, and D have the same tortuosity factor value (higher than for geometry A), despite having quite different morphologies of added dead-end pores. This result highlights that the dead-end pores have no impact on the regular tortuosity value given by eRDM, which is consistent with the fact they do not contribute to the transport through the structure at steady state. In fact, it should be noted that the diffusional flux (from which conventional tortuosity is calculated) is inversely proportional to the MacMullin number (i.e., the same in each case). So even though the dead-end pores do not contribute to species transport at steady-state, their presence does have an effect on the determination of tortuosity, via their additional volume fraction. The identical values for the MacMullin number found by eRDM would imply that the effect of these porous microstructures (mostly the dead-end pores) on the behavior of transport through the pores, is the same regardless of their different pore network morphologies. However, this interpretation would be misleading when modeling battery electrodes, as will be discussed below.

Let us now compare the tortuosities from the eSCM to those of the eRDM described above. In geometry A, when there is only a main through-pore and no dead-end pores added, the tortuosities found by both methods have a good agreement (<1% for relative difference), despite measuring quite different concepts (i.e., flux between parallel boundaries and flux from one boundary to the solid/liquid interface).

As expected, for cases B, C, and D, we find differences in the tortuosities and MacMullin numbers found by the two methods. As discussed, eSCM is a relative measure of how difficult it is to access the solid/liquid interface from one of the boundaries. Firstly, microstructure A has the lowest value of τ_e, so we can think of its surface area as being easy to access, although it doesn't actually have much surface area available. Microstructure B has the highest interfacial surface area, originating from many short dead-end pores. This surface area is slightly harder to access when compared to microstructure A, which is reflected in the value of τ_e; however, it does have over four times as much area available. Microstructure C also has fairly short dead-end pores, but they are much bulkier and there are only two of them. Half of all the additional new surface area is far from the separator, hence a high value of τ_e is observed, and only a modest additional surface area was added anyway. Lastly, microstructure D has a similarly large increase in surface area to case B, but now very long pores must be traveled to access it, so it has the highest tortuosity factor. Importantly, the value of A^* can be observed in the characteristic frequencies of each microstructure through the term C_DL in Eq. 6. The microstructure B and D have the highest values of A^* among all the microstructures, meaning that more time is required to saturate their capacitive surface and hence lower characteristic frequencies are observed.

Figure 4b also contains an inset showing a detailed view of the medium-to-low frequency region (n.b. The high frequency offset on the real axis results from a separator spacer between the two electrodes as illustrated in Fig. 3). As can be seen, for cases B and D, the simulated impedance spectra strongly deviate from the expected shape for the TLM in this region (i.e., 45° slope). The shape of this region is a function of the accessible surface area per unit penetration depth, which explains why A and C are initially identical. Such a signature on the impedance spectra, although being only related to the microstructure, could be misinterpreted as an additional electronic/electrochemical process (e.g., contact resistance between electrode film and current collector or between particles) in experimental symmetric cell impedance measurements.

The discrepancy between τ and τ_e in the results above should not be surprising as the two methods are measuring distinct (but in some cases related) properties of the microstructure. Nevertheless, a key conclusion from the results reported here is that in the case of porous electrodes (i.e., where the pores are pathways for charged species to reach the electrochemical surface area), the more conventional eRDM approach suffers from some key conceptual issues compared to the eSCM approach. In particular, the fact that through-pores and dead-end pores both do participate in the ionic transport during electrode operation, because electrochemical reactions occur at the interfacial area of these pores, contrary to the only "through-pores" scenario in the case of eRDM. Stated more plainly, a battery electrode does not need any pores to percolate all the way from the separator to the current collector in order to function, although this non-percolating scenario would give a value of $\tau = \infty$ if measured with eRDM. Hence, the electrode tortuosity factor, τ_e, obtained from the eSCM seems to be a more appropriate metric to characterize porous electrodes than the tortuosity factor, τ, as eSCM more closely resembles how an actual battery electrode works. However, in the case of an electrode whose particle/feature size was much smaller than the electrode thickness and therefore where the conventional tortuosity factor could be extracted from a subvolume, the eRDM approach may still have some relevance, though it would still suffer from incorrectly accounting for the impact of dead-end pores. Thus, for battery macroscopic models such as Newman's P2D model, the electrode tortuosity factor τ_e should be preferred over the conventional tortuosity factor τ during the parametrization step.

Interestingly, the present results can also reveal information about the likely effect of certain pore morphologies on power performance. For example, if we consider geometries A and B, even though both microstructures show a similar $N_{M,e}$ and R_{ion} (see Eq. 2), the accessible interfacial surface area of pores is not the same, since microstructure B has also the dead-end pores in addition to the through pore. This means that the specific electrochemically active surface area of the microstructure can be increased while keeping a low $N_{M,e}$, which may improve power performance.

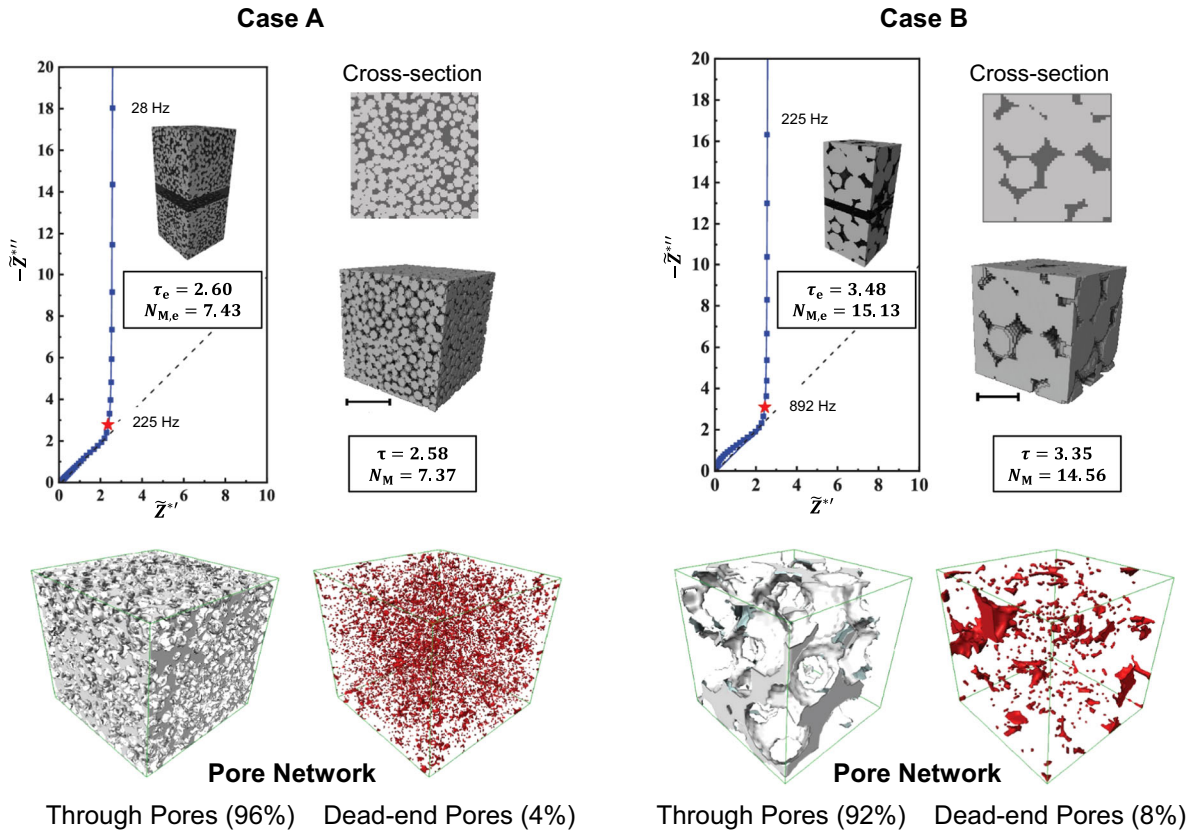

Fig. 5 Comparison of two approaches using two numerically generated 3D microstructures. Case A: microstructure with 2 µm particle size and $\varepsilon = 35\%$. **Case B:** microstructure with 5 µm particle size and $\varepsilon = 20\%$. For each case, a plot shows simulated EIS of eSCM along with the fit using Eq. 4. The high-frequency intercepts with real axis in both cases are different to zero, which represent the ionic resistances from the separator layer. Each plot contains an inset showing the resulting electrode tortuosity factor τ_e and the corresponding symmetric cell configuration. The cross-section and the tortuosity factor τ of these microstructures given by the eRDM are also presented. The pore networks separated into through-pores and dead-end pores are shown. Here, only open pores (connected pores) that possess less than 2% (arbitrary threshold value) of the total flux density are considered as dead-end pores. The threshold value was set to take into account the dead-end pores having either no flux or low flux. The microstructure size in case A is 100 × 100 × 100 voxels, in case B is 50 × 50 × 50 voxels, and the voxel size is 250 nm.

Simulations of 3D microstructures

In this section, we examine 3D microstructures in order to investigate more realistic electrode geometries. Figure 5 shows simulations performed on two 3D microstructures that have small and larger particle size with porosity $\varepsilon = 35\%$ (case A) and $\varepsilon = 20\%$ (case B), respectively. For both cases, the tortuosity factor values were calculated using the two methods and do not show a substantial difference.

Regarding case B, Fig. 5 shows that there is a deviation of the impedance response from the idealized response of the TLM. As mentioned in the previous section, this deviation results from variations in the available surface area per unit penetration depth and as such can be used to indicate one of two relevant concepts. Either the volume being simulated is too small (compared to its characteristic features) to be considered representative of the electrode as a whole; or the microstructure itself is simply not homogenisable (e.g., a graded electrode) and standard porous electrode theory cannot be applied[5,6]. Compared to case A, the particle size in case B is larger, thus the pore details in case B are no longer at a size negligible compared to that of the control volume, suggesting it may not be representative. Even if the full thickness of the electrode is already captured, increasing just the area (i.e., dimensions parallel to the current collector) will also allow for a greater degree of averaging to occur. For example, both the volume fraction and surface area at each distance increment from the current collector may approach a constant value if a large enough area was observed, at which point the simulated EIS response is expected to get closer to the idealized impedance response given by TLM or Newman's P2D model.

This work clearly illustrates how the simulated EIS spectrum for a symmetric cell in blocking condition could be used as a quantitative tool to assess deviation from the porous electrode theory for a particular electrode microstructure. Moreover, when symmetric cell impedance measurements deviate from the expected TLM spectra (as reported in refs [16,19]), this model can help us understand why.

Figure 5 shows two specific cases where there is a good agreement in the tortuosity factor values between the two approaches. The pore networks are highly percolated in both cases (>99%, as expected for packed spheres) and low flux dead-end pores only occupy a minority of the pore networks (4% and 8%, value given by *TauFactor*, for microstructures A and B, respectively), as illustrated in Fig. 5. Hence, the presence of dead-end pores has a minor effect on the tortuosity of the pore networks when eSCM is considered, allowing good agreement with eRDM. Importantly, a significant proportion of the dead-end pores are on the boundaries of the control volumes, suggesting that the dead-end fraction would have decreased further if a larger control volume were considered.

These results show that in case of more realistic 3D microstructures, a reasonable agreement may be obtained between the two approaches. It might also shed light on the

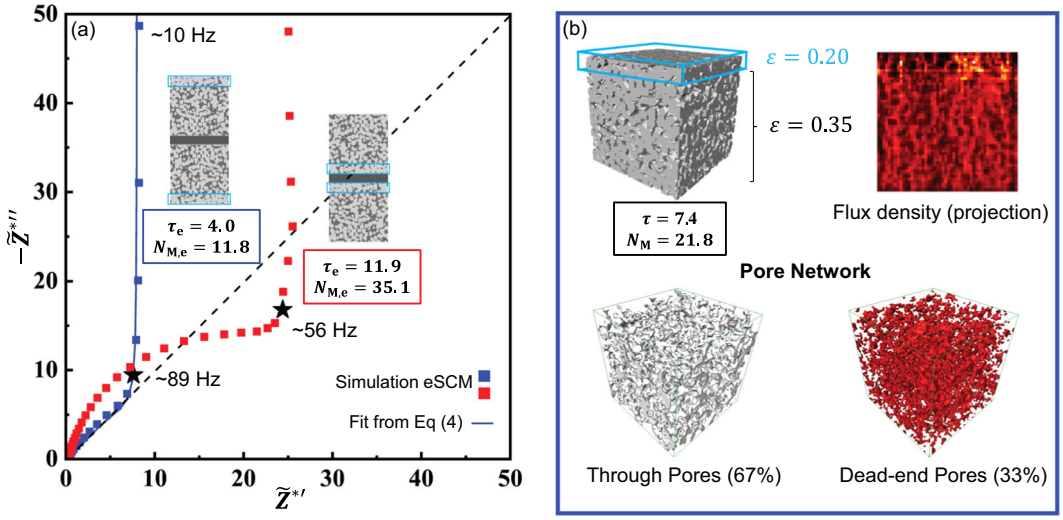

Fig. 6 Illustration of a numerically generated 3D microstructure having two adjacent layers with two different porosities. 90% of volume has $\varepsilon = 35\%$, while 10% (cyan box) of volume has $\varepsilon = 20\%$. **a** The plot shows the simulated EIS of eSCM along with the fit using Eq. 4. The plot contains an inset showing the cross-section of the two microstructures, that have either the lower porosity region at the current collector side (blue square) or at the separator side (red square), in symmetric cell configuration with the associated electrode tortuosity factor τ_e; **b** The 3D microstructure that has lower porosity at the top is shown in detail along with the associated tortuosity factor τ given by eRDM simulation. The simulated flux density shows a lower density on the top corresponding with the lower porosity region. The pore network separated in through-pores and dead-end pores is also presented. The microstructure size is 50 × 50 × 50 voxels, the voxel size equals to 1 μm.

work of Pouraghajan et al.[20], since for commercial electrodes of typical porosity, the pore network might contain mostly through-pores with only small fraction of dead-end pores.

Here, to contrast with the above example, one can imagine a microstructure that has very low porosity, which typically leads to a decrease in the percolation of the pore network and therefore a greater fraction of dead-end pores. In order to showcase this concept, a new 3D microstructure was generated having two adjacent layers with two different porosities. For 90% of the thickness, the porosity is set to 35%, but for the last 10% of its thickness, the porosity is abruptly reduced to 20%, as shown in the cyan box in Fig. 6. The purpose of this is to close most of the pores in order to create an otherwise well-percolated network of long dead-end pores. As a result, some dead-end pores travel almost the entire thickness of the microstructure, thereby increasing the impact of dead-end pores, depending on its orientation relative to the separator/current collector. As such, a substantial difference between the tortuosities measured using the two methods is expected. It is worth-mentioning that the microstructure in this example is potentially an informative and relevant model for some real electrodes, where sub-optimal manufacturing processes can yield a larger electrode density in the region close to the current collector (excess of binder) or the separator (drying too quickly).

In Fig. 6, the volume fraction of dead-end pores in the microstructure (33%) is significantly larger than the microstructure in Fig. 5. These dead-end pores are also larger and better connected across the entire CV. Notably, at the top of the microstructure where the porosity decreases, there are less available through-pores allowing the flux of species all the way through (as measured in eRDM). This effect is illustrated in the projection of simulated flux density from *TauFactor*, also shown in Fig. 6.

Despite having a high conventional tortuosity factor, this pore network, with its relatively large fraction of long, well-percolated, dead-end pores, has most of its surface area easily accessible when the dense region is next to the current collector. This is reflected in the fitted value of $\tau_e = 4.0$, which is much lower than the value of $\tau = 7.4$ calculated for eRDM. However, when the microstructre is reversed, $\tau_e = 11.9$, which is even higher than the eRDM value, highlighting the importance of directional microstructural information absent from conventional flow-through models like eRDM. As mentioned above, electrodes that are dried too quickly during manufacture can have a fairly dense layer of binder near the top, resembling this configuration, and they show poor rate performance.

With the dense layer next to the current collector, the impedance spectrum closely matches the TLM response; however, this is not the case when the dense layer is next to the separator. As already noted, deviations in the medium frequency region of the spectrum are caused by variations in the available surface area per unit penetration depth into the sample. Thus, the spectrum shows more information about these variations the closer they are to the separator, which is also where they would make a greater difference to cell performance. Furthermore, following on from a discussion earlier in the paper, Fig. 6 demonstrates that the homogenisability of an electrode also depends on the analysis direction, which reinforces the conclusions from the simple case of open or closed straight pores in Fig. 3. This directional dependence of the eSCM approach is very informative and clearly reflected in real battery performance data. As such, the electrode tortuosity factor given by the eSCM should be a more appropriate metric for exploring the interplay between the electrode microstructure and cell performance, as it is able to highlight considerations critically lacking from the conventional tortuosity factor as well as various geometric tortuosity definitions. The result in Fig. 6 suggests that graded-porosity designs (with the higher porosity layer at the separator side) could be used to increase the accessible capacity of an electrode, as also shown by Morasch et al.[33]. This design concept was also explored by Lu et al.[34]; however, their analysis was based on geometric tortuosities, which make many simplifications including ignoring path constrictions.

Finally, to understand why τ_e should be used in conventional P2D Newman models instead of τ, it should be understood that single values of the volume fractions, specific surface area and tortuosity factor are typically used to describe a whole electrode. Although it is possible to make each of these values vary as a function of depth (producing a visible effect on the Nyquist plot), the conventional tortuosity factor used to quantify the "obstruction to transport caused by microstructure" refers only to the "flow through" scenario and so is not able to represent anything about

how accessible the surface area is. The tortuosity factor is the only term used to encode microstructural complexity in the P2D model and as such τ_e should be used instead of τ as it more closely represents the scenario in question.

DISCUSSION

Effective transport properties are critical for understanding and modeling battery electrodes. Two main experimental methods exist for determining tortuosity factors (eRDM and eSCM), but they do not always agree. In this study, conceptual flaws are exposed in the use of the conventional tortuosity factor, τ, derived from eRDM for characterizing porous battery electrode materials. In particular, the fact that τ is based on steady-state flow all the way through a system, whereas in a real electrode, ions migrate into the electrode and then onto the active surface area of the electrode itself. A new frequency domain solver was written to simulate the more realistic transport scenario of distributed surface capacitance. This solver (eSCM) has been integrated into the open-source *TauFactor* platform, which already contains a solver for the conventional tortuosity factor (eRDM), and both can be applied directly to segmented tomographic data.

Various synthetic microstructures were generated and then analysed using both tortuosity paradigms to highlight the distinction between the two. Like τ, the electrode tortuosity factor, denoted τ_e, may depend on the orientation of the microstructure (i.e., for anisotropic materials); however, unlike τ, the direction of the analysis can also impact τ_e, which is a concept of particular relevance to graded battery electrode microstructures.

The simulation results from this work unambiguously reveal that dead-end pores are the principal cause of discrepancies between the two approaches. Unlike the conventional "flow through" tortuosity factor where direct pores are optimal ($\tau = 1$), it is demonstrated that τ_e can be less than one, suggesting systems where the interfacial surface area is even easier to access than that of straight pores. As such, eSCM should be preferred over eRDM to be used in Newman's P2D model and/or a TLM to model porous electrodes. Electrochemical modelers should consider this important result at the stage of precise P2D model parametrization.

Finally, this work demonstrates that the impedance spectra simulated from 3D microstructures may deviate from the conventional behavior simulated by a TLM or Newman's P2D model in one of two scenarios: either the control volume is not large enough to be representative of the material, or the system is not conventionally homogeneous, e.g., the accessible interfacial area varies significantly with depth. As well as a qualitative comparison, it is possible to conceive of various metrics that could be used to quantify the degree of agreement between simulated EIS spectrum of the symmetric cell and TLM fit, thus providing a direct way to assess the degree to which porous electrode theory applies to a particular electrode microstructure.

All of these concepts are to be applied to real electrode microstructural data in a follow-up study exploring optimal electrode design.

METHODS

As mentioned above, this work focuses specifically on tortuosity factor determination methods applied to battery porous electrodes. Two methods, eRDM by Thorat et al.[16] and eSCM by Landesfeind et al.[17] and Malifarge et al.[18] are further described and compared in the following sections.

Restricted diffusion method for porous electrodes (eRDM)

Figure 1a shows a schematic of the experimental setup. The cell is first polarized to generate a constant current. Under the applied current, cations are released at one electrode and diffuse/migrate through the three porous layers (separator/free-standing electrode/separator) before finally being consumed at the other electrode. The electric field also causes the electrolyte anions to migrate; however, since the electrodes are blocking with respect to the anions, they accumulate at the positive electrode. This results in a salt concentration gradient across the cell, which in turn results in a concentration overpotential, and a cell potential gradient between two plates. The current is then interrupted and reference electrodes at each side monitor the cell-potential decay during the so-called relaxation step.

During the relaxation process, the migration/diffusion of the ions is obstructed by the porous microstructure of the electrode and separators. A numerical model can then be used to fit the cell-potential decay behavior in order to extract the effective salt diffusion coefficient of the porous layers. For instance, a transport model based on the Mac-Innes equation in a concentrated solution, including migration and diffusion in the liquid phase, can be used[16]. The cell-potential behavior during the polarization step can also be simulated if the model takes into account the charge transfer process at anode and cathode. Hence, it requires knowledge of several intrinsic electrolyte properties rather than just its ionic conductivity, e.g., the transference number and the diffusion coefficient, and also the parameters related to the kinetic reactions at the Li foil interfaces. Finally, using the porosity and tortuosity factors of the separators (which must already be known), it is then possible to isolate the effect of the free-standing electrode and extract its tortuosity factor by numerical fitting.

Symmetric cell method for porous electrodes (eSCM)

The experimental setup for eSCM significantly differs from the eRDM approach and consists of a symmetric cell with two identical electrodes facing each other with a separator in between, as shown in Fig. 1b. The method is based on electrochemical impedance measurements of a symmetric cell in order to determine the effective ionic conductivity of the electrolyte across the porous electrode, which is related to the tortuosity factor of the structure through Eq. 1.

For tortuosity factor determination using eSCM, a so-called blocking (i.e., zero flux) condition is applied at the pore-wall, as no faradaic processes are occurring. In this manner, there is no contribution from charge transfer, or diffusion in either the liquid or solid phases. Another simplifying assumption is that the transport within the separator alone determines the high frequency intercept on EIS spectrum. This means that only processes within the porous electrodes themselves are the cause of the medium and lower frequency EIS data and the effective ionic resistance within the porous electrodes can be determined using a simpler model. The Nyquist plot in Fig. 7a shows an idealized impedance response of a porous electrode in blocking condition. In the medium frequencies, a linear region with a nearly 45° slope results from the distributed capacitance of the double-layer throughout the porous electrode in combination with the ion migration required to access each region of the solid/liquid interface[35–37]. In the low frequencies, the impedance response tends towards a vertical line, typical of an ionically-blocking behavior.

A porous electrode can be represented by a structure with essentially straight-cylindrical pores of uniform diameter, which are homogeneously filled with electrolyte and have a uniformly distributed ionic resistance and double-layer capacitance per unit length. The electrode material is also considered to have uniformly distributed electronic resistance. This porous electrode can then be macroscopically described by a uniform RC transmission line model (TLM), see Fig. 7b[35,38,39]. The electronic resistance of the solid matrix of the electrode and the ionic resistance of the liquid phase are expressed by a serial connection of ohmic resistors, r_{el} and r_{ion}, respectively. In addition, there can be a faradaic and/or capacitive process taking place at the solid/liquid interface, which are described by the surface impedance elements $\bar{z}_t$.

Hence, a system, which consists of two identical TLM (Fig 7b) representing the two porous electrodes along with a simple resistance for the separator layer, can be used to fit the symmetric cell impedance response, allowing for the determination of the effective ionic conductivity which is expressed through the effective resistance of the electrolyte R_{ion} across the electrode[17,19]. This quantity can be further used to determine the tortuosity factor of the electrodes according to the following equation.

$$\frac{\tau_e}{\varepsilon} = \frac{R_{ion} A_{CC} \kappa_0}{L} = N_{M,e}, \tag{2}$$

where $R_{ion} = \Sigma r_{ion}$; L is the electrode thickness (m); A_{CC} is the macroscopic current collector area (m^2); τ_e is the electrode tortuosity factor, which, as discussed in the core of this paper, is distinct from the conventional

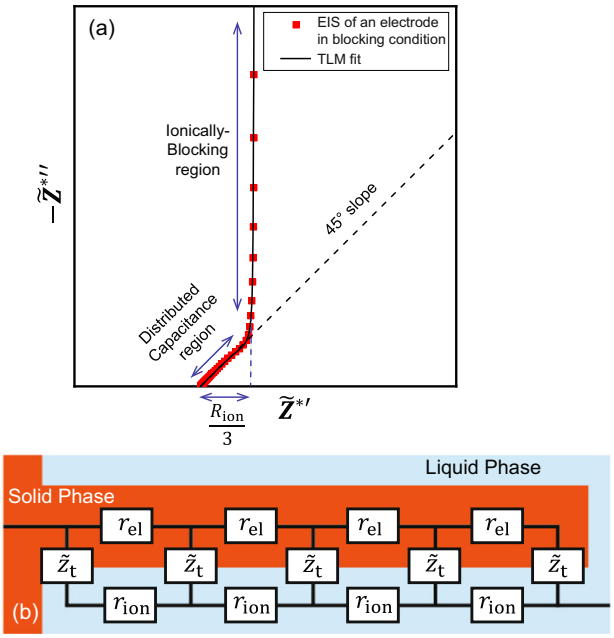

Fig. 7 Impedance theory of the eSCM method. a An ideal impedance response of a porous electrode in blocking condition (no faradaic process so $\tilde{z}_t$ becomes c_{dl} which is the pure capacitance of the double layer) along with the fit using the TLM represented in **b**, which allows the determination of τ_e. Here, since only the impedance of the single electrode is considered, the contribution of the ionic resistance from the separator is not represented in the TLM as well as does not appear in the EIS spectra. The dashed line is used to highlight the 45° slope of the medium frequency region.

tortuosity factor; and $N_{M,e}$ is the Mullin number calculated with the electrode tortuosity factor instead of the conventional tortuosity factor.

Here, we also introduce the relationship between different types of surface areas that are used throughout this work:

$$A^* = \frac{A_{micro}}{A_{CC}} = \frac{aA_{CC}L}{A_{CC}} = aL, \tag{3}$$

where the non-dimensional term A^* is the microscopic active surface area of the electrode per unit of current collector area; A_{micro} is the microstructural active surface area (m^2); a is the volume specific active surface area (m^{-1}).

Landesfeind et al.[17] assumed that the effective electronic resistance of the solid electrode material is much lower than the effective ionic resistance of the electrolyte in the pores so that it can be ignored (i.e., $r_{ion} \gg r_{el} = 0$). In practice, either a highly electronically conductive electrode (such as graphite) must be used, or the experiment should be carried out using an electrolyte with a low enough salt concentration to reduce its ionic conductivity[17,29]. The TLM equation that represents the impedance of a porous electrode can then be simplified to Eq. 4[17,39,40]:

$$\tilde{Z}_{EI} = \sqrt{R_{ion} \cdot \tilde{Z}_t}\coth\left(\sqrt{\frac{R_{ion}}{\tilde{Z}_t}}\right) = \sqrt{\frac{R_{ion}}{j\omega A_{CC}C_{DL}}}\coth\left(\sqrt{j\omega A_{CC}C_{DL}R_{ion}}\right), \tag{4}$$

where $\tilde{Z}_{EI}$ is the porous electrode impedance (Ω); j is the imaginary unit; ω is the radial frequency; $\tilde{Z}_t = \frac{1}{j\omega A_{CC}C_{DL}}$ is the total interfacial impedance (Ω), which, in blocking condition, becomes $C_{DL} = \Sigma c_{dl}\Delta A^*$, the interfacial double layer capacitance per unit current collector area ($F\,m^{-2}$); A^* is defined in Eq. 3, c_{dl} interfacial double layer capacitance per unit microstructural active surface area ($F\,m^{-2}$).

Notably, given the assumptions above, one may realize that the mathematical description of TLM (Eq. 4) reduces to that of a Finite-Space Warburg (FSW) element. Nonetheless, it is worth-mentioning that the parameters governing the behavior are clearly different. The intrinsic capacitances in the two models are not the same, i.e., surface scaling in Eq. 4 instead of volumetric scaling in the case of FSW.

The limiting values of the real and imaginary parts of $\tilde{Z}_{EI}$ as $\omega \to 0$ are shown as follows[40]:

$$\lim_{\omega\to 0}\left(\tilde{Z}'_{EI}\right) = \frac{R_{ion}}{3}. \tag{5}$$

$$\lim_{\omega\to 0}\left(\tilde{Z}''_{EI}\right) = \frac{-1}{\omega A_{CC}C_{DL}}. \tag{6}$$

From Eq. 5, R_{ion} can also be determined approximately since the length of the 45° sloped region spans across approximately $R_{ion}/3$ along the real axis.[19] Likewise, Pouraghajan et al.[20] showed different methods to quickly estimate R_{ion} that all provide a reasonable estimate with minor discrepancy as compared to using the fit of Eq. 4.

In the core of this work, the impedance of the electrode is made dimensionless for ease of comparison by using:

$$\tilde{Z}^*_{EI} = \tilde{Z}_{EI}\frac{A_{CC}\kappa_{eff}}{L}. \tag{7}$$

Malifarge et al.[18] developed a more general analytical expression of the symmetric cell impedance that takes into account an arbitrary electronic resistance of the conductive matrix. More recently, Pouraghajan et al.[20] developed a generalized TLM that takes into account additional possible sources of impedance, such as a contact resistance with the current collector, the charge-transfer resistance, and the electronic resistance of the electrode solid phase.

To better fit the experimental results, the pure capacitance that represents the double layer charging/discharging at the solid/liquid interface can be replaced by Q_S, which denotes a pseudo-capacitance, accompanied by an exponent in the constant-phase element (CPE).

Furthermore, the electrolyte concentration is assumed here to be high enough and the interfacial area not too large, such that we may neglect any significant depletion of ions due to the accumulation of charge in the double layer at the electrode/electrolyte interface. Under this assumption, in addition to the fact that no charge transfer is expected to take place, no concentration gradient is assumed to develop across the cell. Hence, the electrolyte concentration remains uniform throughout. Electrolyte diffusion can thus be safely neglected with the present experimental setup.

It is worth-noting that when charge transfer is blocked in Newman's P2D model, it simplifies down to the TLM[5,6,35,41], which is why the P2D model can also be used to fit the impedance response of the symmetric cell in blocking condition[18]. However, it is restricted to the limiting case where the double layer is a pure capacitance.

Numerical methods—simulation

TauFactor is an open-source MATLAB application developed by Cooper et al.[31] for characterizing microstructure based on image data; including determining the tortuosity factors. In line with the conventional definition of the tortuosity factor, only simple Fickian diffusion is currently solved in *TauFactor*, which is only valid in certain cases, e.g., diffusion of species in an infinitely dilute solution within pores having electrically insulating walls (no double-layer formation). *TauFactor* uses an over-relaxed iterative approach to numerically solve Fick's diffusion equation at steady-state in order to calculate the flux and hence the associated tortuosity factor.

A diffusion simulation can be used to model effective steady-state electronic or thermal conductivity instead, by conceptually replacing the concentration gradient with a potential or temperature gradient respectively, as the mathematics is identical.

To the authors' knowledge, there is currently no numerical tool specifically for modeling the eSCM directly from 3D microstructural data. As such, this critical functionality has now been added to *TauFactor* as a tool for the battery community to highlight the fundamental differences between tortuosities determined by eRDM and eSCM.

While an eRDM model must capture the diffusion of species all the way through a pore network between two parallel boundaries, eSCM considers the migration of a species from the walls of one porous electrode's surface onto the surface of the other electrode (both having a double-layer capacitance). Consequently, there is an extra term that represents the double-layer charging/discharging at the solid/liquid interface within the porous electrodes. Furthermore, the geometry for the simulation now comprises a porous separator layer in between two identical electrode structures to be accounted for, instead of simply a passive (three-layers) porous structure as in the case of eRDM (see Fig. 8). The solid phase of the porous separator is considered to be inert, meaning there is no interaction with either the electrode solid phase or the liquid phase. In a future work,

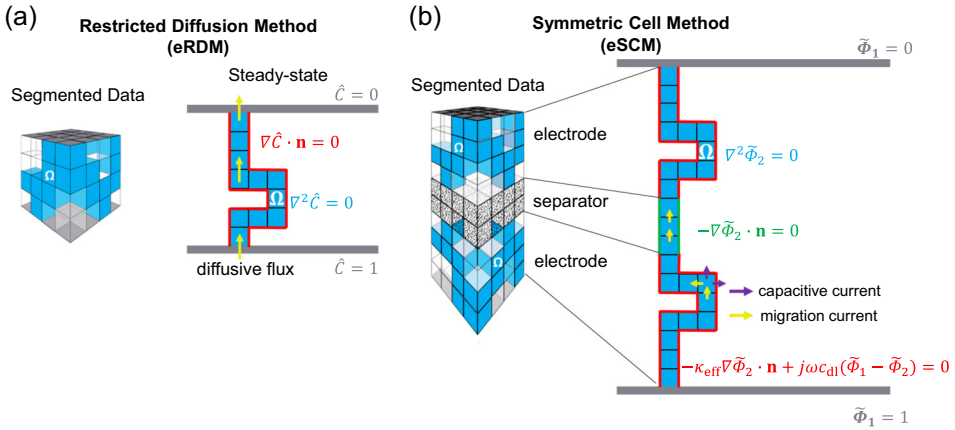

Fig. 8 Illustration of the use of segmented tomographic data as input along with the governing equation and boundary conditions for: **a** eRDM and **b** eSCM simulation implemented in *TauFactor*. Voxels in blue represent the pore network, transparent voxels represent the solid phase. For eRDM, $\hat{C}$ is the complex concentration of the diffusing species. For eSCM, there is a domain in between the two electrodes that represents the porous separator. Since there is no electrochemical reaction occurring in the system, $\tilde{\Phi}_1$ and $\tilde{\Phi}_2$ are simply the electron-conducting phase (solid) and ionic-conducting phase (liquid) electric potentials respectively; ω is the radial frequency of the boundary stimulation; j is the imaginary unit; c_{dl} is the interfacial double layer capacitance per unit microstructural active surface area. For both methods, Ω is the pore network domain in the system (in both electrodes and separator); n is the outward pointing unit normal to each voxel face. The color of the equations corresponds to the domain where they are applied. Vectors are represented in bold.

the 3D model of this symmetric cell structure may be simplified to just a "half-cell", which would be computationally less expensive.

Along with tortuosity determination, Cooper et al. also implemented in *TauFactor* the option to solve this equation in the frequency domain. As a result, one obtains an impedance spectrum of a diffusing species through the pores of an inert (electronically-insulating) porous medium, which can capture the effect of pore structural features that leads to deviations from the conventional Warburg diffusion model[42]. It is worth-noting that the time constants in the diffusion impedance are a volumetric phenomenon, whereas in the eSCM method, they originate from the interfacial capacitance instead. The mathematics correspondence of these two scenarios is described in the appendix of Cooper et al.[42].

In this work, the governing equation of eSCM and its boundary conditions are also Fourier transformed to their frequency domain representation, where sinusoidal stimulation of electric potential typical of EIS becomes a constant value imposed at the boundary, as shown in Fig. 8. As with the other solvers in *TauFactor*, the solver is pre-compiled into C++ and an iterative over-relaxation approach is used to accelerate convergence at each frequency.

We use the symmetric cell model proposed by Landesfeind et al.[17] in which the solid phase of the porous electrode is assumed to have a negligible electronic resistivity, such that its electronic potential is uniform within each electrode. For each frequency, the simulated impedance $\tilde{Z}_{\text{El-sim}}$ is calculated as the ratio of the potential difference between the solid phases of the two electrodes ($\Delta\tilde{\Phi}_1 = 1$ V is arbitrary selected) and the total ionic current density (expressed per geometric cross-sectional area of the cell). Since the physical problem is linear, the value of $\Delta\tilde{\Phi}_1$ has no effect on the simulated impedance and so it is arbitrarily set to unity throughout.

As for the experimental data analysis in ref. [18], the electrode tortuosity is determined from a least-mean square fit of the simulated impedance response to the TLM model using Eq. 4. Practically, the *fminsearch* function in MATLAB is used as the non-linear fitting function to minimize the objective functions shown below:

$$F = \sum_{n=1} \frac{(|\tilde{Z}^*_{\text{El-sim}} - \tilde{Z}^*_{\text{El}}|)^2}{|\tilde{Z}^*_{\text{El-sim}}|^p}, \tag{8}$$

where $\tilde{Z}^*_{\text{El-sim}}$ is the normalized-simulated impedance given by eSCM from *TauFactor*; $\tilde{Z}^*_{\text{El}}$ is the normalized-fitting impedance given by Eq. 4, p is a weighing factor[20]. However, it should be noted that the value of τ_e can be extracted from just the values of $\tilde{Z}^*_{\text{El}}$ at $\omega \to 0$ and $\omega \to \infty$.

Set of studied microstructures

Simulations are run on both 2D and 3D numerically-generated microstructures. The parameters used to simulate the eSCM are given in Table 1.

Table 1. Parameters used in eSCM simulation.

Parameters	Value
κ_0	0.046[1] S m^{-1}
c_{dl} (per unit active surface area)	0.01[2] F m^{-2}
f	$10^7 - 10^{-1}$[a] Hz
Voxel size	$1 \times 1 \times 1$[a] μm^3

[1]The electrolyte conductivity is chosen from ref. [16] for 10 mM blocking electrolyte of salt $TBAClO_4$.
[2]The interfacial double layer capacitance per unit microstructural electrode active surface area is chosen from refs [9,16].
[a]Assumed values.

"Model" 2D microstructures (generated in MS paint) containing simple pore networks are investigated to demonstrate the fundamental difference in terms of the physics and the concept behind the two methods, eRDM and eSCM. Furthermore, 2D microstructures are modified to investigate some specific cases that help unveil the effects of microstructural features such as different morphology of pore networks or different types of pore, on the simulated impedance spectra and/or derived tortuosity value.

For 2D microstructures, we first consider the case where there is a porous separator in which there are only straight pores that perfectly align with those of porous electrodes on both side. For 3D microstructure, to facilitate the data preparation step, we use a free-standing electrolyte layer where only liquid electrolyte is present between the two electrodes with no porous separator. The investigation can also be extended to include the pore network within the separator between the two electrodes in the symmetric cell simulations in future work, since tomographic data of several types of separators are already available in open-access literature[43].

For the 3D structures, random-packing of spheres is generated using GrainGeo module by GeoDict[41] to imitate a battery porous electrode microstructure. Simulations using 3D microstructures allow us to gain insight into the likely behavior of real-life electrodes, given the tomographic data is reliable enough in capturing the real electrode microstructure, and help us shed light on the appropriate method for the determination of tortuosity for battery applications.

DATA AVAILABILITY

The datasets generated and analyzed during the current study are available from the corresponding author on reasonable request.

CODE AVAILABILITY

All codes used in this study have been integrated into the open-source *TauFactor* platform and are available at https://uk.mathworks.com/matlabcentral/fileexchange/57956-taufactor or https://sourceforge.net/projects/taufactor/.

Received: 6 April 2020; Accepted: 17 July 2020;
Published online: 14 August 2020

REFERENCES

1. Goodenough, J. B. Rechargeable batteries: challenges old and new. *J. Solid State Electrochem.* **16**, 2019–2029 (2012).
2. Liu, Y., Zhu, Y. & Cui, Y. Challenges and opportunities towards fast-charging battery materials. *Nat. Energy* **4**, 540–550 (2019).
3. Veneri, O., Ferraro, L., Capasso, C. & Iannuzzi, D. Charging infrastructures for EV: overview of technologies and issues. In *International Conference on Electrical Systems for Aircraft, Railway and Ship Propulsion, ESARS, IEEE* (2012).
4. Botsford, C. & Szczepanek, A. Fast charging vs. slow charging: pros and cons for the new age of electric vehicles. EVS24 International Battery, Hybridand Fuel Cell Electric Vehicle Symposium (2009)
5. Newman, J. & Tiedemann, W. Porous-electrode theory with battery applications. *AIChE J.* **21**, 25–41 (1975).
6. Newman, J. & Thomas-Alyea, K. E. *Electrochemical Systems*. (Wiley-Blackwell, Hoboken, 2012).
7. Taiwo, O. O. et al. Comparison of three-dimensional analysis and stereological techniques for quantifying lithium-ion battery electrode microstructures. *J. Microsc.* **263**, 280–292 (2016).
8. Wood, V. X-ray tomography for battery research and development. *Nat. Rev. Mater.* **3**, 293–295 (2018).
9. Su, Z. et al. X-ray nano-computed tomography in zernike phase contrast for studying 3D morphology of Li-O_2 battery electrode. *ACS Appl. Energy Mater.* **3**, 4093–4102 (2020).
10. Tiedemann, W. & Newman, J. Double-layer capacity determination of porous electrodes. *J. Electrochem. Soc.* **122**, 70 (1965).
11. MacMullin, R. B. & Muccini, G. A. Characteristics of porous beds and structures. *AIChE J.* **2**, 393–403 (1956).
12. Zahn, R., Lagadec, M. F. & Wood, V. Transport in lithium ion batteries: reconciling impedance and structural analysis. *ACS Energy Lett.* **2**, 2452–2453 (2017).
13. Newman, J. & Chapman, T. W. Restricted diffusion in binary solutions. *AIChE J.* **19**, 343–348 (1973).
14. Thompson, S. D. & Newman, J. Differential diffusion coefficients of sodium polysulfide melts. *J. Electrochem. Soc* **136**, 3362 (1989).
15. Harned, H. S. & French, D. M. A Conductance Method for the Determination of the Diffusion Coefficients of Electrolytes. *Ann. N.Y. Acad. Sci.* **46**, 267–284 (1945).
16. Thorat, I. V. et al. Quantifying tortuosity in porous Li-ion battery materials. *J. Power Sources* **188**, 592–600 (2009).
17. Landesfeind, J., Hattendorff, J., Ehrl, A., Wall, W. A. & Gasteiger, H. A. Tortuosity determination of battery electrodes and separators by impedance spectroscopy. *J. Electrochem. Soc.* **163**, A1373–A1387 (2016).
18. Malifarge, S., Delobel, B. & Delacourt, C. Determination of tortuosity using impedance spectra analysis of symmetric cell. *J. Electrochem. Soc.* **164**, E3329–E3334 (2017).
19. Ogihara, N. et al. Theoretical and experimental analysis of porous electrodes for lithium-ion batteries by electrochemical impedance spectroscopy using a symmetric cell. *J. Electrochem. Soc.* **159**, 1034–1039 (2012).
20. Pouraghajan, F. et al. Quantifying tortuosity of porous Li-ion battery electrodes: comparing polarization-interrupt and blocking-electrolyte methods. *J. Electrochem. Soc.* **165**, 2644–2653 (2018).
21. Eastwood, D. S. et al. The application of phase contrast X-ray techniques for imaging Li-ion battery electrodes. *Nucl. Instrum. Methods Phys. Res. Sect. B* **324**, 118–123 (2014).
22. Shearing, P. R. et al. Exploring electrochemical devices using X-ray microscopy: 3D micro-structure of batteries and fuel cells. *Microscopy Anal.* **27**, 19–22 (2013).
23. Julie, V. et al. 3D phase mapping of solid oxide fuel cell YSZ/Ni cermet at the nanoscale by holographic X-ray nanotomography. *J. Power Sources* **243**, 841–849 (2013).
24. Pietsch, P. & Wood, V. X-Ray tomography for lithium ion battery research: a practical guide. *Annu. Rev. Mater. Res.* **47**, 451–479 (2017).
25. Elango, R., Demortière, A., De Andrade, V., Morcrette, M. & Seznec, V. Thick binder-free electrodes for Li-ion battery fabricated using templating approach and spark plasma sintering reveals high areal capacity. *Adv. Energy Mater.* **8**, 1703031 (2018).
26. Zielke, L. et al. Three-phase multiscale modeling of a $LiCoO_2$ cathode: combining the advantages of FIB-SEM imaging and X-ray tomography. *Adv. Energy Mater.* **5**, 1401612 (2015).
27. Hutzenlaub, T. et al. FIB/SEM-based calculation of tortuosity in a porous $LiCoO_2$ cathode for a Li-ion battery. *Electrochem. Commun.* **27**, 77–80 (2013).
28. Usseglio-Viretta, F. L. E. et al. Resolving the discrepancy in tortuosity factor estimation for Li-ion battery electrodes through micro-macro modeling and experiment. *J. Electrochem. Soc.* **165**, A3403–A3426 (2018).
29. Landesfeind, J., Ebner, M., Eldiven, A., Wood, V. & Gasteiger, H. A. Tortuosity of battery electrodes: validation of impedance-derived values and critical comparison with 3D tomography. *J. Electrochem. Soc.* **165**, A469–A476 (2018).
30. Miller, D. J., Proff, C., Wen, J. G., Abraham, D. P. & Bareño, J. Observation of microstructural evolution in li battery cathode oxide particles by in situ electron microscopy. *Adv. Energy Mater.* **3**, 1098–1103 (2013).
31. Cooper, S. J., Bertei, A., Shearing, P. R., Kilner, J. A. & Brandon, N. P. TauFactor: an open-source application for calculating tortuosity factors from tomographic data. *SoftwareX* **5**, 203–210 (2016).
32. Patel, K. K., Paulsen, J. M. & Desilvestro, J. Numerical simulation of porous networks in relation to battery electrodes and separators. *J. Power Sources* **122**, 144–152 (2003).
33. Morasch, R., Landesfeind, J., Suthar, B. & Gasteiger, H. A. Detection of binder gradients using impedance spectroscopy and their influence on the tortuosity of Li-ion battery graphite electrodes. *J. Electrochem. Soc.* **165**, A3459 (2018).
34. Lu, X. et al. 3D microstructure design of lithium-ion battery electrodes assisted by X-ray nano-computed tomography and modelling. *Nat. Commun.* **11**, 1–13 (2020).
35. de Levie, R. On porous electrodes in electrolyte solutions: I. Capacitance effects. *Electrochim. Acta* **8**, 751–780 (1963).
36. Lasia, A. Impedance of porous electrodes. *J. Electroanal. Chem.* **397**, 27–33 (1995).
37. Meyers, J. P., Doyle, M., Darling, R. M. & Newman, J. The impedance response of a porous electrode composed of intercalation particles. *J. Electrochem. Soc.* **147**, 2930–2940 (1988).
38. Keiser, H., Beccu, K. D. & Gutjahr, M. A. Abschätzung der porenstruktur poröser elektroden aus impedanzmessungen. *Electrochim. Acta* **21**, 539–543 (1976).
39. Tröltzsch, U. & Kanoun, O. Generalization of transmission line models for deriving the impedance of diffusion and porous media. *Electrochim. Acta* **75**, 347–356 (2012).
40. ITAGAKI, M. et al. Electrochemical impedance and complex capacitance to interpret electrochemical capacitor. *Electrochemistry* **8**, 649–655 (2007).
41. de Levie, R. On porous electrodes in electrolyte solutions—IV. *Electrochim. Acta* **9**, 1231–1245 (1964).
42. Cooper, S. J., Bertei, A., Finegan, D. P. & Brandon, N. P. Simulated impedance of diffusion in porous media. *Electrochim. Acta* **251**, 681–689 (2017).
43. Lagadec, M. F. Microstructure of Celgard® PP1615 lithium-ion battery separator. *ETH Zurich*. https://doi.org/10.3929/ethz-b-000265085 (2018).

ACKNOWLEDGEMENTS

The authors would like to acknowledge French National Association for Research and Technology (ANRT) for partially supporting the funding of this research work. T.-T.N. was supported by Renault Group for his PhD Project. Authors would like to thank Dr Alexis Rucci for the help to generate the synthetic 3D microstructures used in this work, as well as Dr Nina Meddings and Steve Kench for their contributions to the discussion surrounding this work. S.J.C. was supported by the EPSRC Faraday Institution Multi-Scale Modeling project (https://faraday.ac.uk/;EP/S003053/1, grant number FIRG003).

AUTHOR CONTRIBUTIONS

C.D. proposed the investigation. The work is supervised by C.D., S.J.C., A.D. B.F., and B. D. joined the discussions on the results. T.-T.N. implemented the method and analyzed the results with S.J.C. and C.D. T.-T.N. and S.J.C. wrote the manuscript. All authors revised the paper and approved its final version.

COMPETING INTERESTS

The authors declare no competing interests.

ADDITIONAL INFORMATION

Correspondence and requests for materials should be addressed to C.D. or S.J.C.

Reprints and permission information is available at http://www.nature.com/reprints

Publisher's note Springer Nature remains neutral with regard to jurisdictional claims in published maps and institutional affiliations.